Medical Engineering and Physics 70 (2019) 39–50

Contents lists available at ScienceDirect

Medical Engineering and Physics

journal homepage: www.elsevier.com/locate/medengphy

Computational analysis for non-invasive detection of stenosis in peripheral arteries

Huseyin Enes Salman[a,b,*], Yigit Yazicioglu[b]

[a] Qatar University, Biomedical Research Center, New Research Complex—Zone 5, P.O. Box 2713, Doha, Qatar
[b] Department of Mechanical Engineering, Middle East Technical University, Dumlupinar Street No:1, 06800 Ankara, Turkey

ARTICLE INFO

Article history:
Received 26 July 2018
Revised 24 May 2019
Accepted 10 June 2019

Keywords:
Turbulence-induced vibration
Atherosclerosis
Stenosis
Modal analysis
Biomechanics

ABSTRACT

Atherosclerosis usually affects the entire cardiovascular system, including peripheral blood vessels. Peripheral arterial stenosis may indicate possible serious vascular disorders related to more vital organs. If peripheral arterial stenosis can be discerned at an early stage, it can serve as a warning sign to take precautions, such as using more invasive diagnostic techniques or adopting a healthier life style. In this study, peripheral regions, such as the thigh, upper arm, and neck are modelled considering stenosis of their major arteries. Stenosis generates a fluctuating pressure field on the arterial wall, which leads to vibration on the skin's surface. This stenosis-induced pressure field is modelled as a harmonic load and applied to the inner surface of the arterial structure. The vibration response on bare skin is computationally determined using the superposition of modal responses. Realistic geometries and hyperelastic material properties are used in modelling the layers of skin, fat, muscle, and bones. The results indicate that stenosis severities higher than 70% lead to a considerable increase in vibration-response amplitudes, especially at frequencies greater than 250 Hz. The detailed analysis of skin responses provides useful information to detect the stenosis location, where the sum of the vibration amplitudes attains its maximum value around the stenosis.

1. Introduction

Atherosclerosis is a serious cardiovascular disease that results in inadequate blood supply as a result of fatty material deposits, which promote arterial calcification and thickening. If stenosis exists in coronary arteries feeding the heart, it is called coronary artery disease (CAD), which is one of the leading causes of death worldwide [1]. Occlusion of the arteries feeding the brain is referred to as a Cerebrovascular Accident (CVA), which is the leading cause of adult disability in the United States and Europe [2]. Given the aforementioned facts, diagnosing and treating the stenosed arteries are of critical importance for clinicians. Several invasive methods are clinically applied to detect the location and severity of the stenosis. Arteriography is one of the most important invasive methods and is based on the injection of a roentgen-contrast fluid inside the artery and acquisition of an X-ray image near the suspected site. Fractional flow reserve (FFR) is another invasive procedure that can measure the flow rate and pressure inside a specific coronary artery to understand the hemodynamic significance of the stenosis. For these invasive methods, a thin hollow catheter must be placed through a larger blood vessel to reach the stenosis site.

Non-invasive methods are applied to eliminate the potential risk factors of invasive diagnostic tools. Duplex ultrasound is a radiation-free non-invasive method to evaluate the flow rate inside large arteries such as the carotid and femoral arteries. Ankle Brachial Index (ABI) is another non-invasive method to diagnose a peripheral arterial disease. In this method, the systolic blood pressures at arms and legs are measured and compared using a standard pressure cuff and handheld Doppler instrument. Phonoangiography was first proposed by Lees and Dewey as an alternative non-invasive method that utilizes natural vascular sounds, called murmurs, to gain information about the presence of stenosis [3]. An obstruction inside the artery changes the regular flow behaviour into a chaotic and turbulent form. The turbulent flow is especially noticeable downstream from the stenosis. The resulting turbulence-driven sound and vibration at the post-stenotic region propagate though the surrounding body tissues and reach the skin surface. Recently, Azimpour et al. [4] evaluated these vibroacoustic signals clinically for the detection of CAD by studying 156 patients undergoing elective coronary angiography and stated that the acoustic detection sensitivity and specificity were 0.70 and 0.80 (for stenosis > 50%), respectively. Winther et al. [5] used a

* Corresponding author at: Qatar University, Biomedical Research Center, New Research Complex—Zone 5, P.O. Box 2713, Doha, Qatar.
E-mail addresses: hsalman@qu.edu.qa (H.E. Salman), yigit@metu.edu.tr (Y. Yazicioglu).

https://doi.org/10.1016/j.medengphy.2019.06.007
1350-4533/

similar clinical comparison to identify the diagnostic performance of an acoustic CAD detection system including 1675 patients and reported a sensitivity and specificity of 63 and 44%, respectively.

Coronary arteries can only emit a limited amount of vascular sounds compared to the peripheral arteries. Stenosis-induced coronary artery sounds are suppressed by more powerful natural sounds due to heart-valve closure and breathing. As a result, highly sensitive technology and advanced signal-analysis techniques are required to filter the coronary artery sound. Therefore, we focused on the peripheral arteries, as they provide high arterial sound generation.

Peripheral arterial occlusive disease (PAOD) is defined as a warning sign for serious cardiovascular disorders that can develop in the future. Shammas [6] reported that PAOD patients have 20% higher risk of CAD. Furthermore, Ness and Aronow [7] reported that PAOD patients over 50 years of age have a 42% and 68% incidence of coexistent CVA and CAD, respectively. If an occlusion in a peripheral vessel can be detected, preventive precautions can be taken before observing CAD and CVA.

With the development of sensor technology, it is possible to measure clinically useful information in a cheap and non-invasive manner [8]. The sound and vibration on bare skin can be measured non-invasively using contact or non-contact sensors, and these measurements can provide diagnostically important information [9]. In this study, the radial vibration response on bare skin is investigated, considering the stenosis-driven effects, to better understand the diagnostic features that can be measured by non-invasive instruments. The effects of peripheral arterial stenosis are computationally investigated by employing realistic thigh, upper arm, and neck models.

2. Materials and methods

Vibration analysis can be performed to diagnose medical disorders because altered frequency content may appear for disease cases [10]. In this study, harmonic vibration analysis is performed using the commercial finite-element analysis (FEA) software, ADINA (Watertown, MA). The stenosis-induced harmonic pressure field, which leads to skin vibration, is empirically determined and applied to the inner arterial wall. The problem domain is modelled using the hyperelastic and viscoelastic material properties of the artery and surrounding soft tissues. The dynamic skin response is determined via modal analysis and evaluated from the diagnostic perspective, considering stenosis levels between 50% and 95%.

2.1. Theory and formulation of problem

The employed computational tool utilizes the concept of the vibration of discrete systems to determine the structural responses based on the superposition of modal responses. A discretized system is considered as follows (after [11]):

$$\boldsymbol{M}\ddot{\boldsymbol{u}} + \boldsymbol{C}\dot{\boldsymbol{u}} + \boldsymbol{K}\boldsymbol{u} = \boldsymbol{F}, \tag{1}$$

where $\boldsymbol{M}$ is the system mass matrix, $\boldsymbol{C}$ is the system damping matrix, $\boldsymbol{K}$ is the system stiffness matrix, $\boldsymbol{F}$ is the load vector, and $\boldsymbol{u}$ is the unknown displacement vector.

Linear potential based fluid elements are used in frequency domain analysis for modelling mass properties and wave propagation in the fluid domain. Irrotational, inviscid, and incompressible acoustic fluid elements are employed using the assumption of infinitesimal velocity formulation where the density change and fluid velocity are infinitesimally small. Continuity and energy equations are defined by the fluid velocity potential ϕ, as,

$$\dot{\rho} + \nabla \cdot (\rho \nabla \phi) = 0 \tag{2}$$

$$h = \int \frac{dp}{\rho} = \boldsymbol{\Omega} - \dot{\phi} - \frac{1}{2}\nabla\phi \cdot \nabla\phi \tag{3}$$

where ρ is the fluid density, h is the specific enthalpy, p is the pressure, and $\boldsymbol{\Omega}$ is the body force. Based on the assumption of infinitesimal velocity formulation and neglecting gravity, Eqs. (2) and (3) take the forms

$$\dot{\rho} + \nabla \cdot (\rho \nabla \phi) \approx \dot{\rho} + \rho_0 \nabla^2 \phi \approx \frac{\rho_0 \dot{p}}{B} + \rho_0 \nabla^2 \phi = 0, \tag{4}$$

$$h \approx \frac{p}{\rho_0} \approx -\dot{\phi} \;\rightarrow\; p \approx -\rho_0 \dot{\phi}, \tag{5}$$

where B is the bulk modulus and ρ_0 is the nominal density. Eq. (5) is substituted into Eq. (4) and the final form is obtained:

$$-\rho_0 \ddot{\phi} + B\nabla^2 \phi = 0. \tag{6}$$

Eq. (6) is a special form of the wave equation, which is linear for fluid potential (ϕ) and can be stated in variational form (after [12])

$$-\int_V \rho_0 \ddot{\phi}\delta\phi dV - \int_V B\nabla\phi \cdot \delta\nabla\phi dV - \int_{S_1} B\dot{\boldsymbol{u}} \cdot \boldsymbol{n}\delta\phi dS_1 = 0, \tag{7}$$

where $\boldsymbol{n}$ is the normal vector and S_1 is the fluid-structure interaction surface. The system matrices are defined for Eq. (7) in the following form (after [12]):

$$\begin{bmatrix} 0 & 0 \\ 0 & \boldsymbol{M_{FF}} \end{bmatrix} \begin{bmatrix} \ddot{\boldsymbol{u}} \\ \ddot{\phi} \end{bmatrix} + \begin{bmatrix} 0 & \boldsymbol{C_{FU}^T} \\ -\boldsymbol{C_{FU}} & 0 \end{bmatrix} \begin{bmatrix} \dot{\boldsymbol{u}} \\ \dot{\phi} \end{bmatrix} + \begin{bmatrix} 0 & 0 \\ 0 & \boldsymbol{K_{FF}} \end{bmatrix} \begin{bmatrix} \boldsymbol{u} \\ \phi \end{bmatrix} = 0, \tag{8}$$

where $\boldsymbol{M_{FF}}$ is the matrix from the $\ddot{\phi}\delta\phi$ term, $\boldsymbol{K_{FF}}$ is the matrix from the $\nabla\phi \cdot \delta\nabla\phi$ term, and $\boldsymbol{C_{FU}}$ is the matrix from the $\dot{\boldsymbol{u}} \cdot \boldsymbol{n}\delta\phi$ term. The fluid medium and structure are directly coupled by combining Eqs. (1) and (8) in the following form:

$$\begin{bmatrix} \boldsymbol{M} & 0 \\ 0 & \boldsymbol{M_{FF}} \end{bmatrix} \begin{bmatrix} \ddot{\boldsymbol{u}} \\ \ddot{\phi} \end{bmatrix} + \begin{bmatrix} \boldsymbol{C} & \boldsymbol{C_{FU}^T} \\ -\boldsymbol{C_{FU}} & 0 \end{bmatrix} \begin{bmatrix} \dot{\boldsymbol{u}} \\ \dot{\phi} \end{bmatrix} + \begin{bmatrix} \boldsymbol{K} & 0 \\ 0 & \boldsymbol{K_{FF}} \end{bmatrix} \begin{bmatrix} \boldsymbol{u} \\ \phi \end{bmatrix} = \begin{bmatrix} \boldsymbol{F} \\ 0 \end{bmatrix}. \tag{9}$$

The structural harmonic displacement response $\boldsymbol{u}$ (i.e., $\boldsymbol{u} = \boldsymbol{U}e^{i\omega t}$ where $\boldsymbol{U}$ is the amplitude), can be determined by solving the set of equations in the matrices provided in Eq. (9). The harmonic velocity response $\dot{\boldsymbol{u}}$ is

$$\dot{\boldsymbol{u}} = i\omega\boldsymbol{u}, \tag{10}$$

where ω is the angular frequency and $i = \sqrt{-1}$. The natural frequencies and corresponding mode shapes of the system are determined within the frequency range of interest by employing the Lanczos method, which is suggested for large problems containing potential-based fluid elements [13]. Eq. (9) is numerically solved using ADINA (Watertown, MA) to determine the harmonic responses in the solid domain.

2.2. Acoustic pressure field in constricted artery

In a constricted pipe, the flow field can be divided into five zones, as shown in Fig. 1. The first zone is upstream of the stenosis, where laminar flow is observed with low noise generation unless the critical Reynolds number is not exceeded [14–16]. In the second zone, the flow area decreases and the axial flow velocity significantly increases. After the stenosis is passed over, flow separation occurs in the third zone, in which a flow jet is formed, and recirculating flow is observed near the artery wall [17–19]. The third zone is highly turbulent, and the highest vascular sound is generated in this zone. In the fourth zone, the flow reattaches the wall, and if the artery is long enough, flow stabilization and

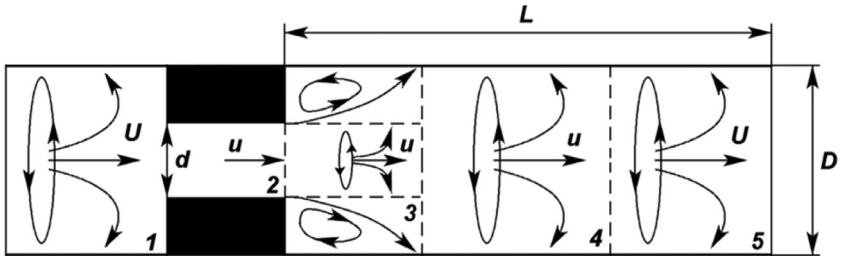

Fig. 1. Flow zones observed in a constricted pipe (after Borisyuk [14]).

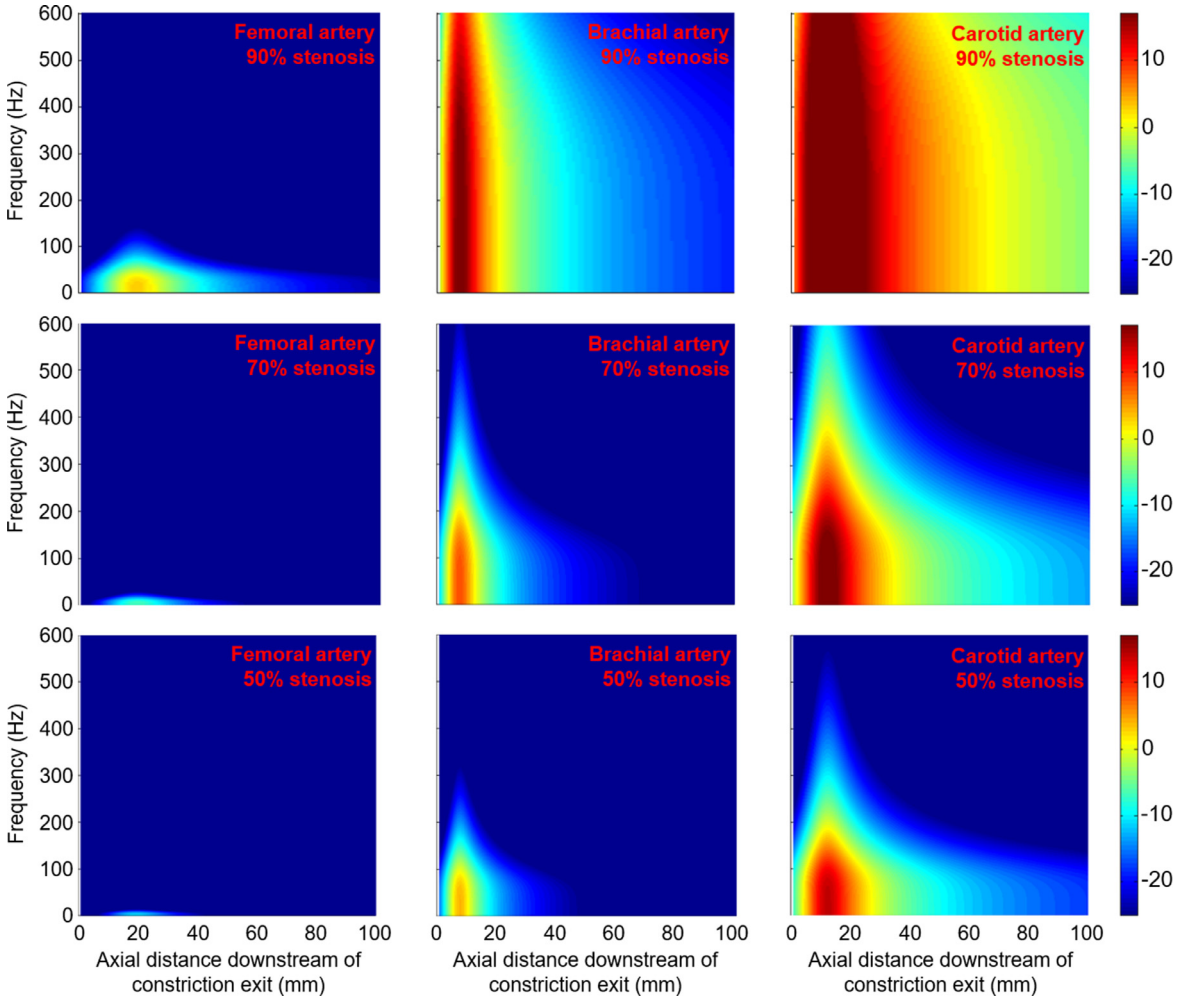

Fig. 2. Acoustic pressure (dB reference: 1 Pa) fields as function of axial position and frequency. Pressure fields are obtained at peak blood flow rates for 50, 70, and 90% stenosis in the femoral, brachial, and common carotid arteries. The stenosis exit is located at 0 mm.

redevelopment are observed in the fifth zone. In our study, only the downstream of the stenosis is modelled, owing to this region's high vibro-acoustic generation.

Turbulent pressure fluctuations are the main cause of vascular sound generation. In this study, we determined and implemented these pressure fluctuations using empirical equations based on the experimental findings of Tobin and Chang [20]. They proposed a general parameter set to obtain the acoustic pressure field in steady pipe flow considering different stenosis severities and flow rates. Using these empirical equations, acoustic pressure fluctuations in the arterial wall are determined using considerably less computational power than in computational fluid dynamics (CFD) analysis.

Yazicioglu et al. [21] used Eq. (11) to define the relationship between the acoustic pressure amplitude and frequency. In Eq. (11), p denotes the acoustic pressure amplitude, ρ denotes the density of the fluid medium, U denotes the flow velocity at unconstricted region, f denotes the frequency, x denotes the distance downstream the stenosis exit, and D and d are the unconstricted and constricted lumen diameters, respectively. At the stenosis exit, the lumen diameter of the artery increases to the nominal value (D). $F_{n1}[x/D]$ is a nondimensional parameter that defines the relation between the acoustic pressure amplitude and distance to the stenosis exit.

$$p[x] = 1.82F_{n1}[x/D]\rho U^{3/2} \cdot \frac{D^{5/2}}{d^2}\left(\frac{1}{1+20\left(fd^2/UD\right)^{5.3}}\right)^{1/2} \quad (11)$$

The arterial flow velocity continuously varies between systole and diastole. Because the highest amplitude sound is generated at the instant of highest blood flow rate, we focused on the quasi-

steady solution at peak flow velocity. The peak flow velocities are 150, 650, and 1200 mm/s for the femoral, brachial, and common carotid arteries, respectively [22,23].

The lumen diameters are approximately 10, 4, and 6.4 mm for the femoral, brachial, and common carotid arteries, respectively [24–26]. The applied peak flow rates and lumen diameters correspond to Reynolds numbers of 750, 1300, and 3840 in the femoral, brachial, and common carotid arteries, respectively. By using the peak blood flow rates and anatomical arterial diameters in Eq. (11), stenosis-induced acoustic pressure fields are obtained as shown in Fig. 2. The decrease in the stenosis level gradually diminishes the acoustic pressure amplitudes. The greatest arterial sound generation is observed in neck due to the high blood flow rate, whereas the least sound is generated in the femoral artery as a result of having the lowest flow rate. The phase difference is neglected in the acoustic pressure field. In our previous study, the artery model is surrounded by soft tissue, and it is concluded that the effect of the phase difference is negligible in the presence of the surrounding tissue [27].

2.3. Modelling the geometry of anatomical regions

The upper arm, thigh, and neck are modelled considering the artery, blood, muscle, fat, skin, and bone layers. Two different modelling approaches are considered in this work: idealized simple geometric models and computed tomography (CT)-based realistic models. Open-access CT data provided by OsiriX DICOM image library (Bernex, Switzerland) were used to obtain three-dimensional models. Idealized models are created for the upper arm and thigh by inspecting the real cross-sectional views of these anatomical regions. The geometrical dimensions of the anatomical regions differ depending on the gender, age, and body weight of the individual. Therefore, the selected average dimensions are used to create idealized models. The thicknesses of tissue layers are set as uniform for the idealized models. CT-based models are created utilizing patient-specific data of the upper arm, thigh, and neck regions. The CT images are processed using Mimics (Materialise, Leuven, Belgium) segmentation software to distinguish the tissue layers by colour scales. The idealized and CT-based models are presented in Fig. 3.

The idealized upper arm model has a uniform outer diameter of 80 mm, total length of 140 mm, fat thickness of 6 mm, and skin thickness of 2 mm [28]. The brachial artery thickness, as reported by Suessenbacher et al. [29], is treated as 0.4 mm in the idealized upper arm model. The idealized thigh model has a total length of 250 mm with a diameter decreasing from 160 to 120 mm. As reported in the study of Smilde et al. [30], 0.75 mm is used as the femoral artery thickness in the idealized thigh model. The total lengths and diameters of the idealized and CT-based models are similar and comparable. The CT-based neck model has a length of 70 mm, outer diameter of approximately 100 mm, fat thickness of 4 mm, skin thickness of 2 mm, and common carotid artery thickness of 0.7 mm [31].

To achieve mesh independent results, three different mesh densities are considered for each anatomical region. Eight-node hexahedral elements are used for all layers of the models. The moderate mesh density provides satisfactorily accurate results in terms of the spectral content and amplitudes of the dynamic skin response. A sample case is solved and evaluated for the CT-based neck model with 90% stenosis severity to prove the mesh independence of the obtained results. The difference of mean radial velocity response amplitude (within 0–60 mm and 0–350 Hz) is found as 3.61% between the moderate and high mesh densities. For each anatomical model, a moderate mesh density is used to obtain the presented results. In Table 1, the total number of elements is listed for each anatomical model considering light, moderate, and high mesh densities.

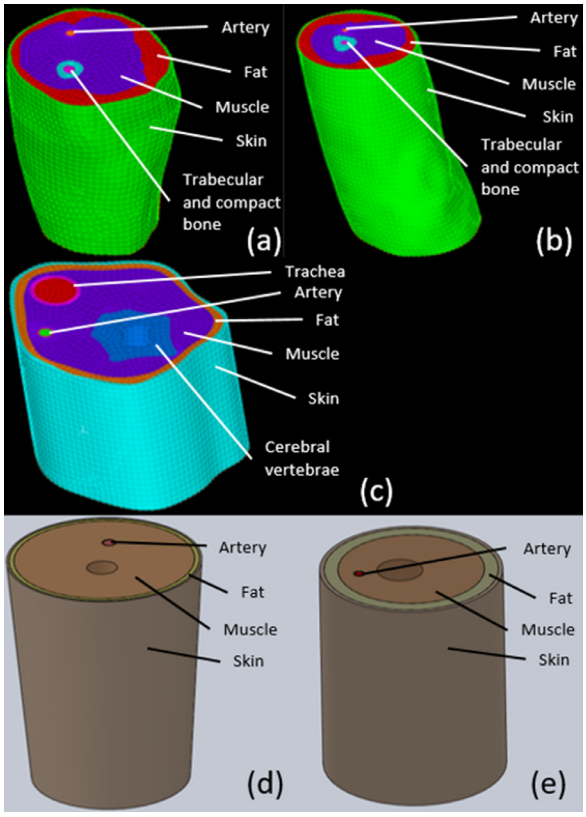

Fig. 3. Idealized and CT-based models. From outside to centre, layers are in the form of skin, fat, muscle, and bone. For the CT-based thigh and upper arm models, trabecular and compact bone structures are considered separately. (a) CT-based thigh model. (b) CT-based upper arm model. (c) CT-based neck model. Trachea (pink) and air (red) are considered only for the neck model. (d) Idealized thigh model. (e) Idealized upper arm model.

Table 1
Total element numbers for different mesh densities.

Anatomical model	Light mesh density	Moderate mesh density	High mesh density
Idealized thigh	53,947	95,116	135,188
Idealized upper arm	65,527	91,215	140,779
CT-based thigh	52,078	73,429	105,856
CT-based upper arm	55,564	84,991	141,390
CT-based neck	34,052	66,295	114,567

The two end surfaces of all anatomical models are fixed by setting no displacement, considering the high stiffness of biological tissues at the joint ends. The artery and blood are directly coupled at the fluid-structure interaction interface. All structural layers are connected to adjacent tissues as though bonded without any slippage. For idealized models, the bones are assumed as rigid and the bone layers are not modelled, owing to their higher stiffness compared with soft body tissues. Therefore, the boundary surfaces of the bones are fixed with no displacement in the idealized models. The harmonic pressure load presented in Fig. 2 is radially applied along the inner arterial wall. Three different damping coefficients are used, namely, light (2% modal damping), medium (10% modal damping), and high (20% modal damping), to account for the variability in damping for each individual depending on age, tissue structure, and body fat [32].

Table 2
Material properties employed in models (Poisson's ratio: ν; Elastic modulus: E; Ogden material parameters: μ_1, μ_2, μ_3, μ_4, α_1, α_2, α_3, α_4; Mooney–Rivlin material parameters: c_{10}, c_{01}, c_{11}, c_{20}, c_{30}).

Material	Model	Density (ρ) (kg/m^3)	Bulk modulus (B) (GPa)	Material parameters			
Acoustic fluid [36]		1000	2.2				
Fat [37]	Ogden	1000	2.2	$\mu_1 = 23,\ 583$ Pa	$\mu_2 = 40$ Pa	$\mu_3 = -40,\ 878$ Pa	$\mu_4 = 19,\ 340$ Pa
				$\alpha_1 = -2.0623$	$\alpha_2 = 25$	$\alpha_3 = -3.4784$	$\alpha_4 = -4.4864$
Skin [37]	Ogden	1000	2.2	$\mu_1 = 6375.4$ Pa	$\mu_2 = 180$ Pa	$\mu_3 = -3770.7$ Pa	$\mu_4 = 1840$ Pa
				$\alpha_1 = 1.3416$	$\alpha_2 = 25$	$\alpha_3 = -7.8671$	$\alpha_4 = -10.898$
Muscle [38]	Mooney–Rivlin	1000	2.2	$c_{10} = 10,\ 000$ Pa		$c_{20} = 10,\ 000$ Pa	$c_{30} = 6666.7$ Pa
Femoral artery [39]	Mooney–Rivlin	1000	2.2	$c_{10} = 18,\ 900$ Pa	$c_{01} = 2750$ Pa	$c_{20} = 590,\ 420$ Pa	$c_{11} = 857,\ 180$ Pa
Brachial artery [40]	Linear elastic	1086		$\nu = 0.49$	$E = 3.8$ MPa		
Common carotid artery [41]	Mooney–Rivlin	1000	2.2	$c_{10} = 94,\ 600$ Pa			
Trachea [42]	Linear elastic	1000		$\nu = 0.499$	$E = 1.66$ MPa		
Compact bone [43]	Linear elastic	2000		$\nu = 0.3$	$E = 15$ GPa		
Trabecular bone [43]	Linear elastic	1100		$\nu = 0.3$	$E = 0.6$ GPa		

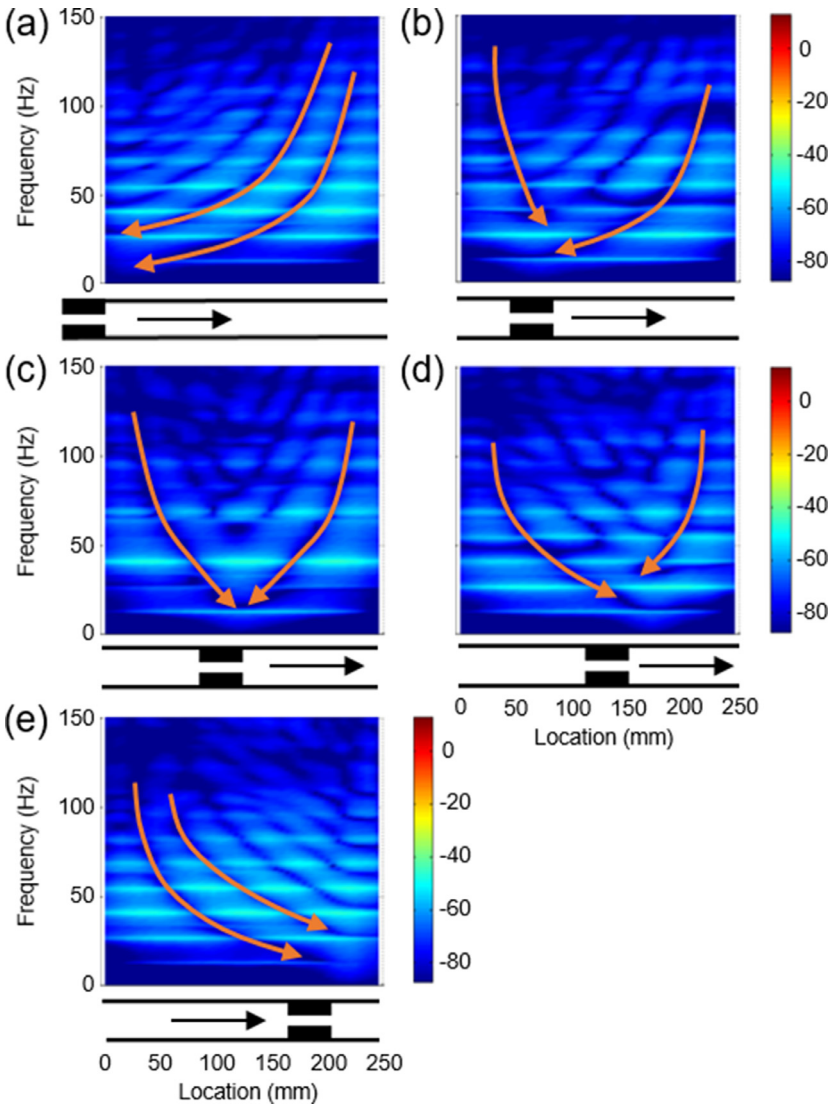

Fig. 4. Radial velocity response (dB reference: 1 mm/s) as a function of axial distance and frequency for the idealized thigh model with 90% stenosis. Stenosis locations are represented under each plot and aligned with the horizontal axis. Flow direction is from left to right, as indicated by arrows. Samples of anti-resonance curves intersecting around the stenosis location are represented using orange curves. (a) Stenosis exit at 0 mm. (b) Stenosis exit at 50 mm. (c) Stenosis exit at 125 mm. (d) Stenosis exit at 150 mm. (e) Stenosis exit at 200 mm.

Table 3
Viscoelastic parameters employed in models (Maxwell viscoelastic parameters: $\boldsymbol{\beta}_1$, $\boldsymbol{\beta}_2$, $\boldsymbol{\beta}_3$, $\boldsymbol{\beta}_4$, $\boldsymbol{\beta}_5$; Relaxation time: $\boldsymbol{\tau}_1$, $\boldsymbol{\tau}_2$, $\boldsymbol{\tau}_3$, $\boldsymbol{\tau}_4$, $\boldsymbol{\tau}_5$).

	β_1	β_2	β_3	β_4	β_5	$\tau_1\,(s)$	$\tau_2\,(s)$	$\tau_3\,(s)$	$\tau_4\,(s)$	$\tau_5\,(s)$
Fat [37]	0.493	0.427				0.3834	4.6731			
Skin [37]	0.288	0.712				0.2136	8.854			
Muscle [44]	2.0216	0.519	0.1125	0.433	0.2424	0.6	6	30	60	300
Artery [45]	0.353	0.286	0.298	0.285	0.348	0.001	0.01	0.1	1	10

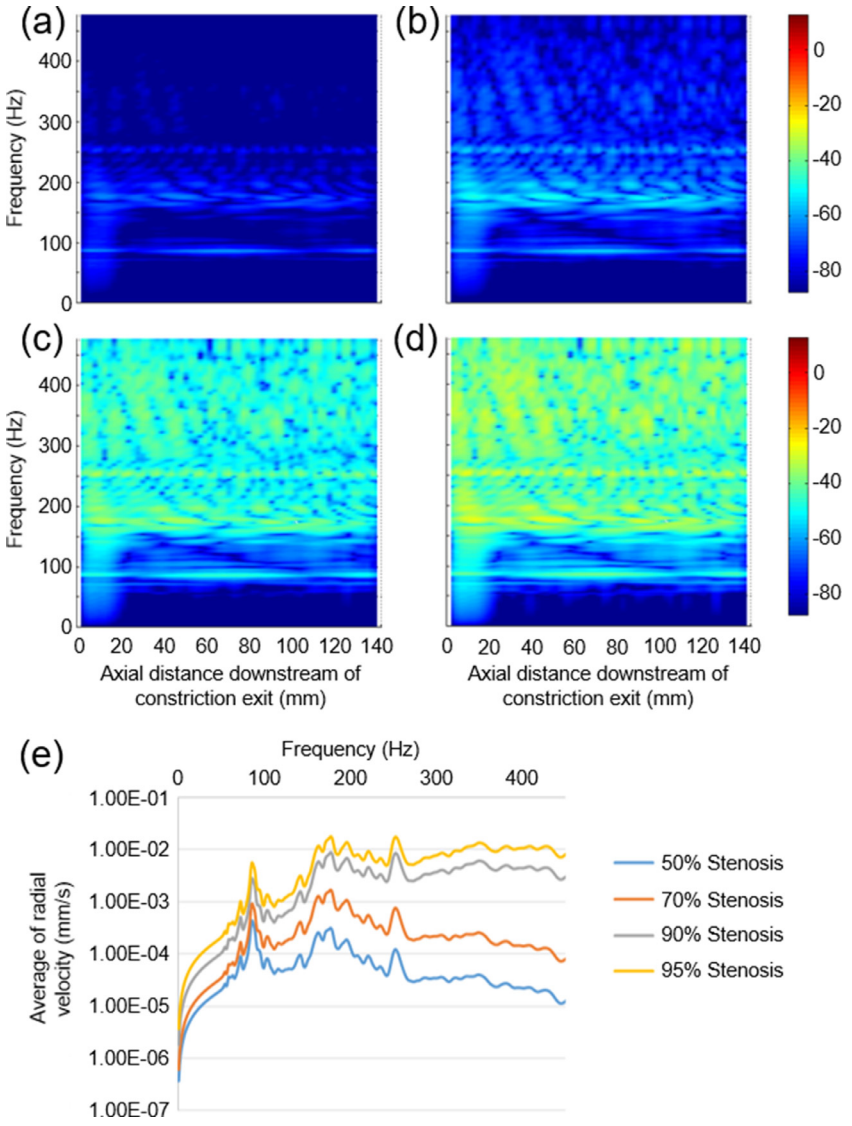

Fig. 5. Radial velocity response (dB reference: 1 mm/s) as a function of axial distance and frequency for the idealized upper arm model. Stenosis exit is placed at 0 mm. (a) 50% stenosis. (b) 70% stenosis. (c) 90% stenosis. (d) 95% stenosis. (e) Average radial velocity response for the idealized upper arm model. For each frequency, the response amplitudes within 0–140 mm are averaged.

2.4. Material properties

Realistic material properties are employed in both idealized and CT-based models considering hyperelasticity and viscoelasticity. For skin, fat, artery and muscle, nonlinearly elastic material properties are employed to define the relation between stress and strain using hyperelastic Ogden and Mooney–Rivlin approaches. Bones are modelled as linearly elastic in CT-based models considering the trabecular and compact bone layers. For the Mooney–Rivlin hyperelastic model [33,34], the strain energy density function is defined by Eq. (12).

$$W = c_{10}(I_1-3) + c_{01}(I_2-3) + c_{20}(I_1-3)^2 + c_{02}(I_2-3)^2 + c_{11}(I_1-3)(I_2-3) + c_{30}(I_2-3)^2 + c_{03}(I_2-3)^3 + c_{21}(I_1-3)^2(I_2-3) + c_{12}(I_1-3)(I_2-3) + D_1(J-1)^2 \quad (12)$$

In Eq. (12), W is the strain energy per unit volume; J is the volume ratio; c_{10}, c_{01}, c_{20}, c_{02}, c_{11}, c_{30}, c_{03}, c_{21}, c_{12}, and D_1 are the material parameters; and I_1 and I_2 are the first and second strain invariants. For the Ogden hyperelastic model [35], the strain energy density function (W) is defined as in Eq. (13).

$$W = \sum_{i=1}^{N} \frac{\mu_i}{\alpha_i}\left(\lambda_1^{\alpha_i} + \lambda_2^{\alpha_i} + \lambda_3^{\alpha_i} - 3\right) + \sum_{i=1}^{N} \frac{1}{D_1}(J-1)^{2i} \quad (13)$$

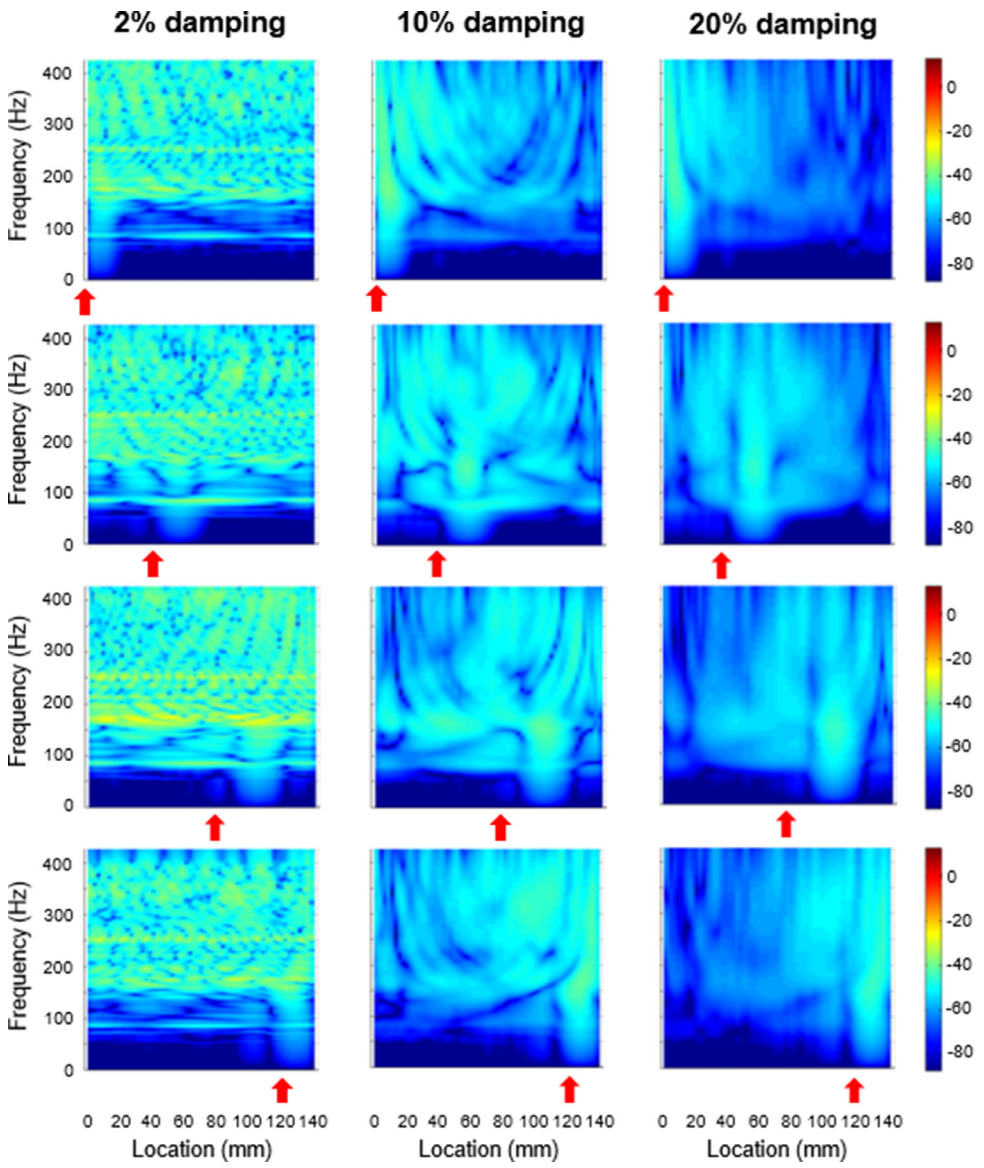

Fig. 6. Radial velocity response (dB reference: 1 mm/s) for the idealized upper arm model with 90% stenosis considering various stenosis locations and modal damping coefficients. The modal damping coefficients are 2%, 10%, and 20% in the left, middle, and right columns, respectively. Four different stenosis exit locations are considered: 0, 40, 80, and 120 mm, as shown by arrows below each response plot.

In Eq. (13), N is the number of polynomials; $\lambda_1^{\alpha_i}$, $\lambda_2^{\alpha_i}$, and $\lambda_3^{\alpha_i}$ are the principle stretches, and μ_i, α_i, and D_1 are the material parameters.

The viscoelastic material behaviour of soft body tissues is modelled using the generalized Maxwell approach, where the relaxation modulus is defined using the Prony series expression as described by Eq. (14).

$$E(t) = E^{\infty}\left[1 + \sum_{\alpha=1}^{N} \beta^{\alpha} e^{\left(-\frac{t}{\tau^{\alpha}}\right)}\right] \tag{14}$$

In Eq. (14), N is the number of Maxwell elements, E^{∞} is the long-term elastic modulus, E^{α} is elastic coefficient, β^{α} is viscoelastic parameter, and τ^{α} is the relaxation time. β^{α} and E^{∞} are determined using Eqs. (15) and (16), respectively. All material properties and viscoelastic parameters are summarized in Tables 2 and 3, respectively.

$$\beta^{\alpha} = \frac{E^{\alpha}}{E^{\infty}} \tag{15}$$

$$E^{\infty} = 1 - \sum_{\alpha=1}^{N} E^{\alpha} \tag{16}$$

3. Results and discussion

The radial velocity response on the skin surface is investigated to locate the stenosis and observe the influence of stenosis severity. The frequency range of interest is 0–150 Hz for the thigh and 0–400 Hz for the upper arm and neck. The amplitude of skin vibration significantly decreases beyond the specified frequency ranges. The effects of stenosis are only observed up to 150 Hz in the thigh because of the low blood flow rate. For all anatomical models, the highest skin-response amplitudes are expected at the closest radial distance to the diseased artery. Therefore, the skin nodes located at the radially closest distance are of primary interest. The results are indicated in a coloured dB scale using a reference velocity of 1 mm/s. For all radial velocity response plots, the same colour scale (−87.5 to 12.5 dB) is used for ease of comparison.

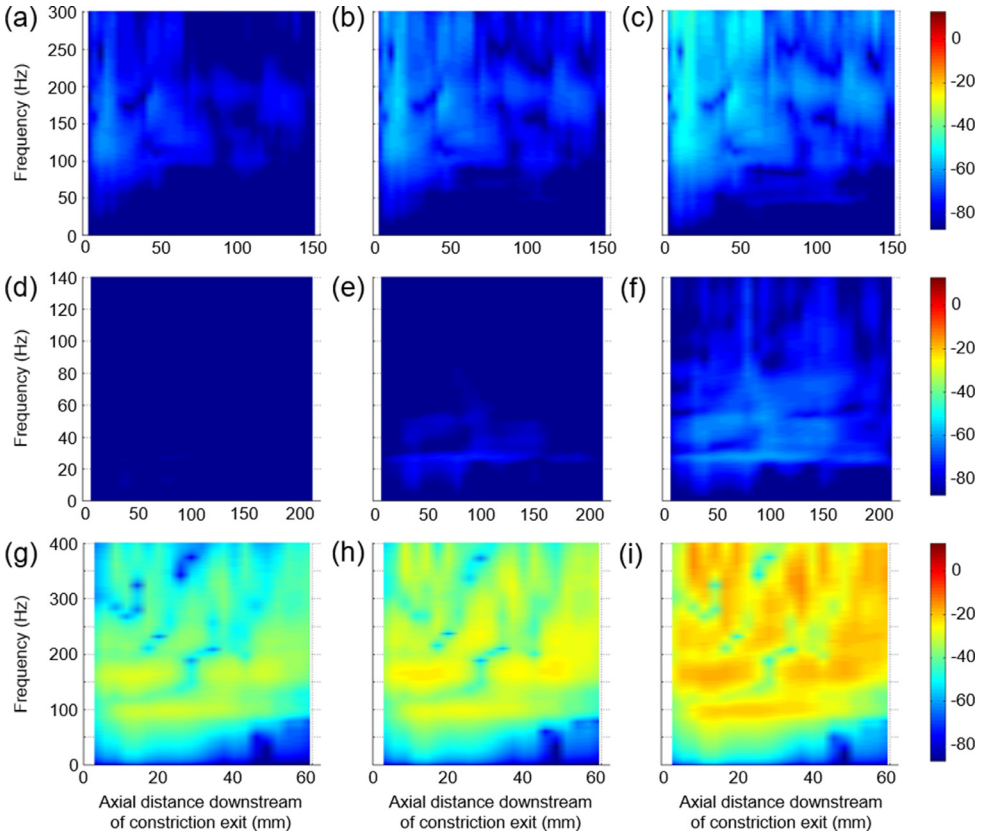

Fig. 7. Radial velocity response (dB reference: 1 mm/s) as a function of axial distance and frequency for CT-based models considering 10% modal damping. Stenosis exit is placed at 0 mm. (a) Upper arm, 70% stenosis. (b) Upper arm, 80% stenosis. (c) Upper arm, 90% stenosis. (d) Thigh, 70% stenosis. (e) Thigh, 80% stenosis. (f) Thigh, 90% stenosis. (g) Neck, 70% stenosis. (h) Neck, 80% stenosis. (i) Neck, 90% stenosis.

In Fig. 4, the effect of stenosis location is investigated for the idealized thigh model. The first, second, and third natural frequencies are observed at approximately 15, 30, and 45 Hz, respectively. The amplitude scales of the response plots do not significantly change with different stenosis locations. However, the spectral content of the plots vary significantly with stenosis location. On the response plots, the regions with the lowest amplitudes are called anti-resonance points. The locus of the anti-resonance points can be used to create anti-resonance curves, as shown in Fig. 4. Anti-resonance curves provide critical information because they tend to intersect near the location of the stenosis.

In Fig. 5, the radial velocity responses are presented for the idealized upper arm model considering various stenosis severities in the brachial artery. The increase in severity leads to an increase in the response amplitudes. The spectral content of the response plot is not as simple that of the idealized thigh model. It is difficult to distinguish the anti-resonance curves in the idealized upper arm responses. As the geometry of the model becomes more complex, the detection of anti-resonance curves becomes more challenging. In Fig. 5(e), the amplitude increase due to stenosis severity does not have a linear trend. The increase in amplitude is not critical at stenosis up to 70%, but severities greater than 70% lead to a major increase in the skin response. Clinically, flow disorders may occur in the case of mild stenosis (50%), but for skin vibration, the observed threshold is 70% stenosis. The average amplitudes in Fig. 5(e) indicate that the influence of stenosis severity is more dominant at frequencies higher than 250 Hz. For the low-frequency range, between 0 and 250 Hz, resonant peaks of the anatomical models are more dominant and suppress the stenosis-induced effects. The amplitude increase with severity becomes more prominent at high frequencies (>250 Hz), and this general amplitude increase is an indication of the presence of stenosis.

Heretofore, a 2% modal damping coefficient is employed to consider light damping conditions. In Fig. 6, the effects of medium (10%) and high (20%) modal damping are investigated in the idealized upper arm model. As the damping increases, the radial velocity response plots become more blurred and the amplitudes slightly decrease; however, the location of the stenosis is more clearly observed. In the case of high damping, it is difficult to detect anti-resonance curves due to blurring of the response plots. However, increased damping facilitates the determination of the stenosis location, because high amplitudes are observed near the stenosed region.

In Fig. 7, the radial velocity responses are presented for CT-based thigh, upper arm, and neck models considering various stenosis severities. CT-based geometries are more complex than idealized models. Therefore, there is a difference in response amplitudes between the idealized and CT-based models. Anti-resonance curves are not visible on CT-based response plots. In Fig. 8, skin response plots are provided for the CT-based thigh model considering light damping (2% modal damping). Even in light damping conditions, the change in stenosis location does not have a significant effect on the response plots, and anti-resonance curves cannot be distinguished for the CT-based models. For this reason, an alternative approach is utilized to gain information about the stenosis location. The amplitudes between 0 and 300 Hz are summed at each spatial location and a two-dimensional plot is obtained for each response plot. Two-dimensional plots illustrating the sum of response amplitudes are presented in Fig. 9. These amplitude sums reach the maximum value around the stenosis location for both idealized and CT-based upper arm models. Using the

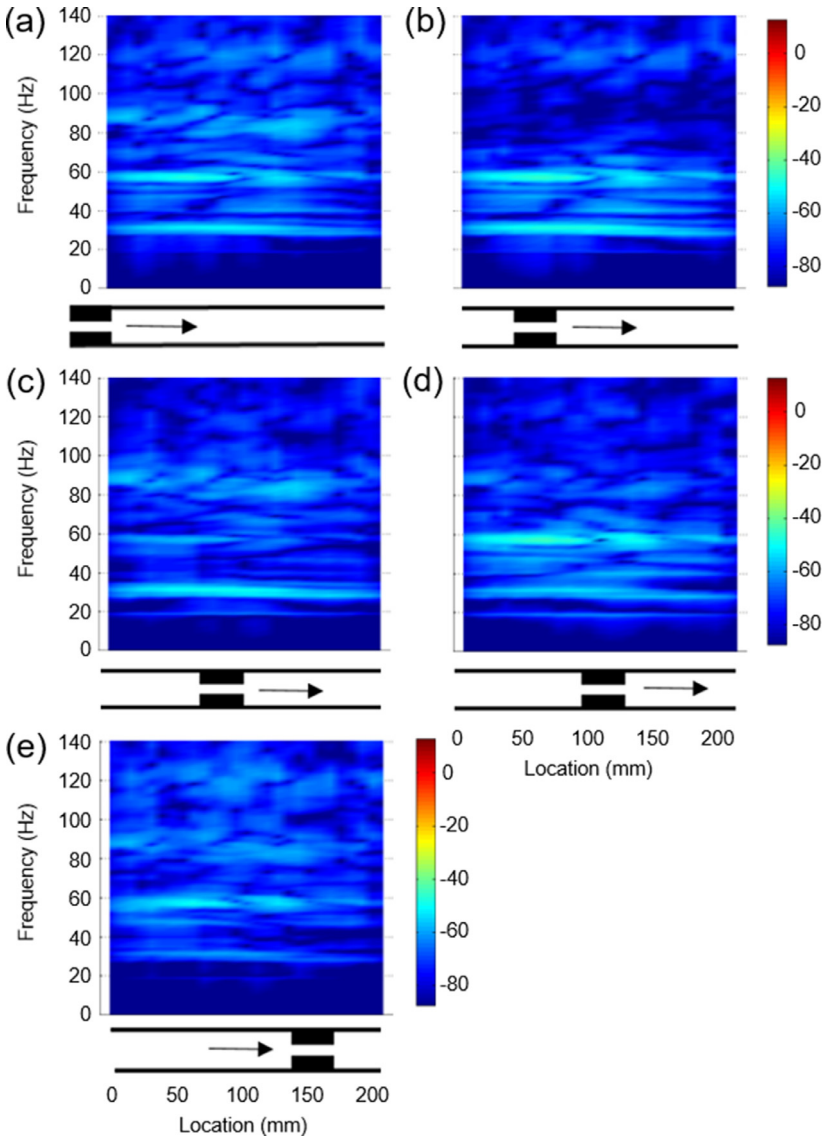

Fig. 8. Radial velocity response (dB reference: 1 mm/s) as a function of axial distance and frequency for CT-based thigh model with 90% stenosis and 2% modal damping. Stenosis locations are represented under each plot and aligned with the horizontal axis. Flow direction is from left to right, as shown by arrows. (a) Stenosis exit at 0 mm. (b) Stenosis exit at 75 mm. (c) Stenosis exit at 100 mm. (d) Stenosis exit at 125 mm. (e) Stenosis exit at 175 mm.

amplitude sums, the stenosis location can be determined in high damping conditions or in cases where the anti-resonance curves cannot be distinguished. The stenosis location can be more clearly defined for the idealized models because of their decreased geometric complexity.

4. Limitations

Under large deformation conditions, muscle fibres align in a certain direction, which results in anisotropic behaviour. In this study, the anisotropic characteristics of muscle are neglected for small strains, as turbulence-induced acoustic pressures result in quite small deformations. Thus, muscle fibres have a crimped structural form that can be modelled as nearly isotropic for small strains (<2%) [46].

Because the turbulence-induced acoustic pressure amplitudes are determined using empirical equations based on experimental findings, the stenosis shape and length are assumed to be same as in the study by Tobin and Chang [20]. The stenosis element has a total length of 12.7 mm with a blunt constriction profile. In reality, arterial stenosis may have a curved profile with a certain eccentricity. In our study, the empirical equations are only limited to a concentric stenosis profile with a steady flow condition. In physiological pulsatile flow, the flow rate changes instantly, which scales the acoustic generation up and down. We mainly consider the instant of peak flow velocity for its high sound generation. Once the acoustic generation is obtained for an instant, the acoustic pressure map can also be predicted for other phases of pulsatile cardiac cycle by scaling the amplitudes depending on the flow rate. Cassanova and Giddens [47] stated that the pressures generated by steady and pulsatile flows are similar in terms of amplitudes; however, the pulsatile flow generates more homogeneous spectra due to the diffusion of turbulence during deceleration of the blood flow in the diastolic phase.

Blood is modelled using water material properties [15,16,20,21], as the mass properties and wave propagation inside blood are mainly considered for the acoustic fluid elements employed in frequency-domain analysis. The artery is modelled as a single-layer structure by neglecting the effect of its multiple layers. Muscle, fat, and skin are modelled as bonded tissues without any slippage. The

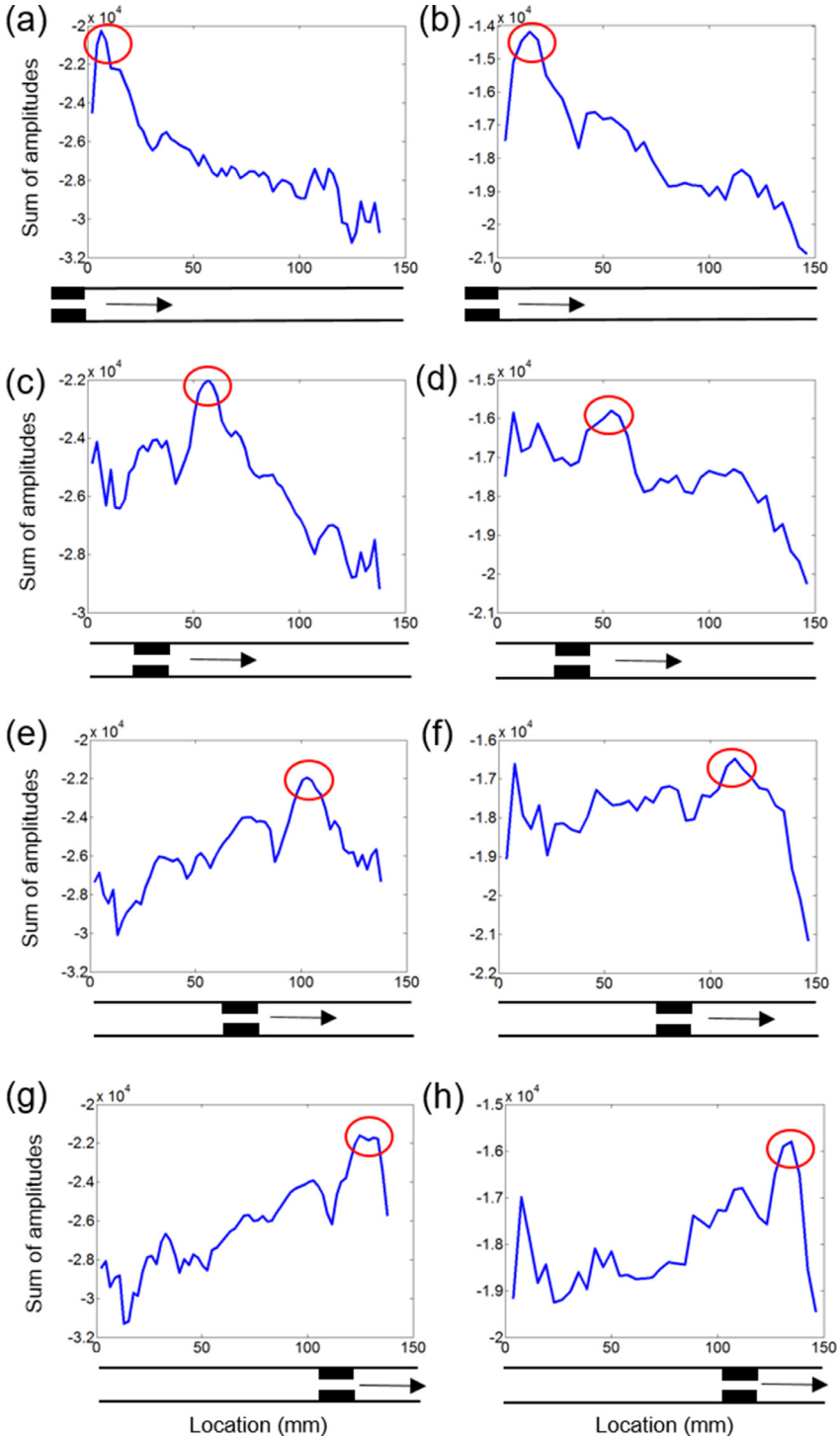

Fig. 9. Sum of response amplitudes for upper arm models considering 90% stenosis and 10% modal damping. Stenosis locations are represented under the plots and aligned with the horizontal axis. (a) Idealized model, stenosis exit at 0 mm. (b) CT-based model, stenosis exit at 0 mm. (c) Idealized model, stenosis exit at 40 mm. (d) CT-based model, stenosis exit at 47 mm. (e) Idealized model, stenosis exit at 80 mm. (f) CT-based model, stenosis exit at 93 mm. (g) Idealized model, stenosis exit at 120 mm. (h) CT-based model, stenosis exit at 117 mm.

stenosis-induced acoustic pressure field is determined considering the mean lumen diameter of the artery, and arterial diameter variation is neglected.

In our modelling approach, several parameters are defined specifically to model the hyperelastic and viscoelastic material properties of the tissue layers. These parameters may vary to a certain extent for each patient, and an amplitude difference can be observed for each case. However, these amplitude differences in the dynamic skin response, related to the modelling assumptions and variations in parameters, are considered to be limited and are not expected to change the main conclusions of this study.

5. Conclusion

In this work, stenosed upper arm, thigh, and neck models are investigated diagnostically using skin vibration responses. The

acoustic pressures generated at the downstream of stenosis exit are modelled using empirical equations and applied to the inner arterial wall. In the anatomical models, the artery is surrounded by muscle, fat, and skin layers. Realistic model geometries are used by utilizing open-access CT data. The hyperelastic and viscoelastic material properties of soft body tissues are implemented in the models. The radial velocity vibration responses are computationally determined on the outer skin surface. It is observed that increasing the stenosis severity results in nonlinearly increasing response amplitudes. The critical threshold is 70% stenosis severity, as occlusions greater than 70% result in a drastic increase in skin vibration. This severity-based amplitude increase is more pronounced at frequencies greater than 250 Hz. Anti-resonance curves are distinguished for the idealized thigh model, and these curves intersect near the stenosis location. As the model geometry becomes more complex in CT-based models, the anti-resonance curves are not clearly visible. For this reason, an alternative approach is employed based on the sum of the radial velocity response amplitudes within the frequency range of interest. The sum of amplitudes attains the maximum value near the stenosis location. In both the idealized and CT-based models, the amplitude sums indicate the location of stenosis.

Conflict of interest

The authors have no financial or personal conflicts of interest to be declared.

Ethical approval

Not required.

Acknowledgments

This work is internally supported by Middle East Technical University (METU) Scientific Research Project (BAP) under grant number BAP-03-02-2015-006. The authors would like to thank BTech Innovation (Ankara, Turkey) for providing technical support for the reconstruction of the three-dimensional models. The authors would also like to acknowledge the financial support from the Turkish Scientific and Technical Research Council (TUBITAK) under the 2211/C program.

Supplementary materials

Supplementary material associated with this article can be found, in the online version, at doi:10.1016/j.medengphy.2019.06.007.

References

[1] Thomas T, Nancy H, Wayne R, Virginia JH, John R, Teri M, et al. Heart disease and stroke Statistics—2006 update. Circulation 2006;113:e85–151. doi:10.1161/CIRCULATIONAHA.105.171600.
[2] Feigin VL. Stroke epidemiology in the developing world. Lancet 2005;365:2160–1. doi:10.1016/S0140-6736(05)66755-4.
[3] Lees RS, Dewey CF. Phonoangiography: a new noninvasive diagnostic method for studying arterial disease. Proc Natl Acad Sci 1970;67:935 LP-942. doi:10.1073/pnas.67.2.935.
[4] Azimpour F, Caldwell E, Tawfik P, Duval S, Wilson RF. Audible coronary artery stenosis. Am J Med 2016;129:515–21 e3. doi:10.1016/j.amjmed.2016.01.015.
[5] Winther S, Nissen L, Schmidt SE, Westra JS, Rasmussen LD, Knudsen LL, et al. Diagnostic performance of an acoustic-based system for coronary artery disease risk stratification. Heart 2018;104:928 LP-935. doi:10.1136/heartjnl-2017-311944.
[6] Shammas NW. Epidemiology, classification, and modifiable risk factors of peripheral arterial disease. Vasc Health Risk Manag 2007;3:229–34.
[7] Ness J, Aronow WS. Prevalence of coexistence of coronary artery Disease, ischemic Stroke, and peripheral arterial disease in older Persons, mean age 80 Years, in an academic hospital-based geriatrics practice. J Am Geriatr Soc 1999;47:1255–6. doi:10.1111/j.1532-5415.1999.tb05208.x.
[8] Guala A, Camporeale C, Ridolfi L, Mesin L. Non-invasive aortic systolic pressure and pulse wave velocity estimation in a primary care setting: an in silico study. Med Eng Phys 2017;42:91–8. doi:10.1016/j.medengphy.2017.02.007.
[9] Jeger-Madiot N, Gateau J, Fink M, Ing R-K. Non-contact and through-clothing measurement of the heart rate using ultrasound vibrocardiography. Med Eng Phys 2017;50:96–102. doi:10.1016/j.medengphy.2017.09.003.
[10] Alshuhri AA, Holsgrove TP, Miles AW, Cunningham JL. Development of a non-invasive diagnostic technique for acetabular component loosening in total hip replacements. Med Eng Phys 2015;37:739–45. doi:10.1016/j.medengphy.2015.05.012.
[11] Clough RW, Penzien J. Dynamics of structures. 1993. Copyr Appl Mech Mater 1993.
[12] Olson LG, Bathe K-J. Analysis of fluid-structure interactions. a direct symmetric coupled formulation based on the fluid velocity potential. Comput Struct 1985;21:21–32. doi:10.1016/0045-7949(85)90226-3.
[13] Bathe K-J, Wilson EL. Solution methods for eigenvalue problems in structural mechanics. Int J Numer Methods Eng 1973;6:213–26. doi:10.1002/nme.1620060207.
[14] Borisyuk AO. Modeling of noise generation by a vascular stenosis †. Int J Fluid Mech Res 2002;29:3–18.
[15] Borisyuk AO. Model study of noise field in the human chest due to turbulent flow in a larger blood vessel. J Fluids Struct 2003;17:1095–110. doi:10.1016/S0889-9746(03)00056-2.
[16] Borisyuk AO. Experimental study of wall pressure fluctuations in rigid and elastic pipes behind an axisymmetric narrowing. J Fluids Struct 2010;26:658–74. doi:10.1016/j.jfluidstructs.2010.03.005.
[17] Back LH, Roschke EJ. Shear-layer flow regimes and wave instabilities and reattachment lengths downstream of an abrupt circular channel expansion. J Appl Mech 1972;39:677–81.
[18] Crow SC, Champagne FH. Orderly structure in jet turbulence. J Fluid Mech 1971;48:547–91 doi:. doi:10.1017/S0022112071001745.
[19] Abdallah SA, Hwang NHC. Arterial stenosis murmurs: an analysis of flow and pressure fields. J Acoust Soc Am 1988;83:318–34. doi:10.1121/1.396433.
[20] Tobin RJ, Chang I-D. Wall pressure spectra scaling downstream of stenoses in steady tube flow. J Biomech 1976;9:633–40. doi:10.1016/0021-9290(76)90105-6.
[21] Yazicioglu Y, Royston TJ, Spohnholtz T, Martin B, Loth F, Bassiouny HS. Acoustic radiation from a fluid-filled, subsurface vascular tube with internal turbulent flow due to a constriction. J Acoust Soc Am 2005;118:1193–209. doi:10.1121/1.1953267.
[22] Gayathri K, Shailendhra K. Pulsatile blood flow in large arteries: comparative study of burton's and mcdonald's models. Appl Math Mech 2014;35:575–90. doi:10.1007/s10483-014-1814-7.
[23] Holdsworth DW, Norley CJD, Frayne R, Steinman DA, Rutt BK. Characterization of common carotid artery blood-flow waveforms in normal human subjects. Physiol Meas 1999;20:219–40. doi:10.1088/0967-3334/20/3/301.
[24] Chami HA, Keyes MJ, Vita JA, Mitchell GF, Larson MG, Fan S, et al. Brachial artery diameter, blood flow and flow-mediated dilation in sleep-disordered breathing. Vasc Med 2009;14:351–60. doi:10.1177/1358863X09105132.
[25] Sandgren T, Sonesson B, Ahlgren ÅR, Länne T. The diameter of the common femoral artery in healthy human: influence of sex, age, and body size. J Vasc Surg 1999;29:503–10. doi:10.1016/S0741-5214(99)70279-X.
[26] Krejza J, Arkuszewski M, Kasner SE, Weigele J, Ustymowicz A, Hurst RW, et al. Carotid artery diameter in men and women and the relation to body and neck size. Stroke 2006;37:1103–5. doi:10.1161/01.STR.0000206440.48756.f7.
[27] Salman HE, Yazicioglu Y. Flow-induced vibration analysis of constricted artery models with surrounding soft tissue. J Acoust Soc Am 2017;142:1913–25. doi:10.1121/1.5005622.
[28] Jain SM, Pandey K, Lahoti A, Rao PK. Evaluation of skin and subcutaneous tissue thickness at insulin injection sites in Indian, insulin naïve, type-2 diabetic adult population. Indian J Endocrinol Metab 2013;17:864–70. doi:10.4103/2230-8210.117249.
[29] Suessenbacher A, Dörler J, Wunder J, Hohenwarter F, Alber HF, Pachinger O, et al. Comparison of brachial artery wall thickness versus endothelial function to predict late cardiovascular events in patients undergoing elective coronary angiography. Am J Cardiol 2013;111:671–5. doi:10.1016/j.amjcard.2012.11.020.
[30] Smilde TJ, van den Berkmortel FW, Boers GH, Wollersheim H, de Boo T, van Langen H, et al. Carotid and femoral artery wall thickness and stiffness in patients at risk for cardiovascular disease, with special emphasis on hyperhomocysteinemia. Arterioscler Thromb Vasc Biol 1998;18:1958–63. doi:10.1161/01.atv.18.12.1958.
[31] Simons PC, Algra A, Bots ML, Grobbee DE, van der Graaf Y. Common carotid intima-media thickness and arterial stiffness: indicators of cardiovascular risk in high-risk patients. The SMART study (Second manifestations of ARTerial disease). Circulation 1999;100:951–7.
[32] Gupta M, Gupta TC. Modal damping ratio and optimal elastic moduli of human body segments for anthropometric vibratory model of standing subjects. J Biomech Eng 2017;139:101006–13.
[33] Mooney M. A theory of large elastic deformation. J Appl Phys 1940;11:582–92. doi:10.1063/1.1712836.
[34] Rivlin RS, Saunders DW. Large elastic deformations of isotropic materials VII. Experiments on the deformation of rubber. Philos Trans R Soc Lond Ser A, Math Phys Sci 1951;243:251–88. doi:10.1098/rsta.1951.0004.
[35] William OR, Rodney H. Large deformation isotropic elasticity–on the correlation of theory and experiment for incompressible rubberlike solids. Proc R Soc Lond A Math Phys Sci 1972;326:565–84. doi:10.1098/rspa.1972.0026.

[36] Salman HE, Sert C, Yazicioglu Y. Computational analysis of high frequency fluid–structure interactions in constricted flow. Comput Struct 2013;122:145–54. doi:10.1016/j.compstruc.2012.12.024.
[37] Wu JZ, Dong RG, Welcome DE. Analysis of the point mechanical impedance of fingerpad in vibration. Med Eng Phys 2006;28:816–26. doi:10.1016/j.medengphy.2005.11.013.
[38] Meier P, Blickhan R. FEM-simulation of skeletal muscle: the influence of inertia during activation and deactivation. Skeletal muscle mechanical from mechanical to functions. Chicester: John Wiley & Sons, Ltd; 2000.
[39] Prendergast PJ, Lally C, Daly S, Reid AJ, Lee TC, Quinn D, et al. Analysis of prolapse in cardiovascular Stents: a constitutive equation for vascular tissue and finite-element modelling. J Biomech Eng 2003;125:692–9.
[40] Leguy CAD, Bosboom EMH, Gelderblom H, Hoeks APG, van de Vosse FN. Estimation of distributed arterial mechanical properties using a wave propagation model in a reverse way. Med Eng Phys 2010;32:957–67. doi:10.1016/j.medengphy.2010.06.010.
[41] Liu H, Canton G, Yuan C, Yang C, Billiar K, Teng Z, et al. Using in vivo cine and 3D multi-contrast MRI to determine human atherosclerotic carotid artery material properties and circumferential shrinkage rate and their impact on stress/strain predictions. J Biomech Eng 2012;134:11008–9.
[42] Webster MR, De Vita R, Twigg JN, Socha JJ. Mechanical properties of tracheal tubes in the american cockroach (Periplaneta americana). Smart Mater Struct 2011;20:94017. doi:10.1088/0964-1726/20/9/094017.
[43] Untaroiu C, Darvish KK, Crandall JR, Deng B, Wang J-T. Characterization of the lower limb soft tissues in pedestrian finite element models. Proc Int Tech Conf Enhanc Saf Veh 2005;2005 8p–8p.
[44] Van Loocke M, Lyons CG, Simms CK. Viscoelastic properties of passive skeletal muscle in compression: stress-relaxation behaviour and constitutive modelling. J Biomech 2008;41:1555–66. doi:10.1016/j.jbiomech.2008.02.007.
[45] Holzapfel GA, Gasser TC, Stadler M. A structural model for the viscoelastic behavior of arterial walls: continuum formulation and finite element analysis. Eur J Mech - A/Solids 2002;21:441–63. doi:10.1016/S0997-7538(01)01206-2.
[46] Freutel M, Schmidt H, Dürselen L, Ignatius A, Galbusera F. Finite element modeling of soft tissues: material models, tissue interaction and challenges. Clin Biomech 2014;29:363–72. doi:10.1016/j.clinbiomech.2014.01.006.
[47] Cassanova RA, Giddens DP. Disorder distal to modeled stenoses in steady and pulsatile flow. J Biomech 1978;11:441–53. doi:10.1016/0021-9290(78)90056-8.